OXFORD

Human Molecular Genetics, 2015, Vol. 24, No. 22 6515–6529

doi: 10.1093/hmg/ddv360
Advance Access Publication Date: 11 September 2015
Original Article

ORIGINAL ARTICLE

Vapb/Amyotrophic lateral sclerosis 8 knock-in mice display slowly progressive motor behavior defects accompanying ER stress and autophagic response

Frédérique Larroquette[1,†], Lesley Seto[1,†], Perrine L. Gaub[1], Brishna Kamal[1], Deeann Wallis[2], Roxanne Larivière[1], Joanne Vallée[3], Richard Robitaille[3] and Hiroshi Tsuda[1,*]

[1]Department of Neurology and Neurosurgery, Montreal Neurological Institute, McGill University, Montreal, Quebec, Canada H3A 2B4, [2]Department of Biochemistry and Biophysics, Texas A&M University, Cypress, TX, USA and [3]Departement of Neurosciences, University of Montreal, Montreal, Quebec, Canada

*To whom correspondence should be addressed. Tel: +514 3985720; Fax: +514 3981509; Email: hiroshi.tsuda@mcgill.ca

Abstract

Missense mutations (P56S) in *Vapb* are associated with autosomal dominant motor neuron diseases: amyotrophic lateral sclerosis and lower motor neuron disease. Although transgenic mice overexpressing the mutant vesicle-associated membrane protein-associated protein B (VAPB) protein with neuron-specific promoters have provided some insight into the toxic properties of the mutant proteins, their role in pathogenesis remains unclear. To identify pathological defects in animals expressing the P56S mutant VAPB protein at physiological levels in the appropriate tissues, we have generated *Vapb* knock-in mice replacing wild-type *Vapb* gene with P56S mutant *Vapb* gene and analyzed the resulting pathological phenotypes. Heterozygous P56S *Vapb* knock-in mice show mild age-dependent defects in motor behaviors as characteristic features of the disease. The homozygous P56S *Vapb* knock-in mice show more severe defects compared with heterozygous mice reflecting the dominant and dose-dependent effects of P56S mutation. Significantly, the knock-in mice demonstrate accumulation of P56S VAPB protein and ubiquitinated proteins in cytoplasmic inclusions, selectively in motor neurons. The mutant mice demonstrate induction of ER stress and autophagic response in motor neurons before obvious onset of behavioral defects, suggesting that these cellular biological defects might contribute to the initiation of the disease. The P56S *Vapb* knock-in mice could be a valuable tool to gain a better understanding of the mechanisms by which the disease arises.

Introduction

Amyotrophic lateral sclerosis (ALS) is a fatal, typically late-onset neurodegenerative disorder associated with the dysfunction or death of motor neurons. Unfortunately, there is no primary therapy for this disease and its pathogenesis is poorly understood. The disease is most often sporadic, but about 10% of the patients inherit the disease (1). Currently, mutations in almost 20 genes including *vesicle-associated membrane protein-associated protein B* (*VAPB*, ALS8), *Superoxide dismutase 1* (*SOD1*), *TAR DNA binding protein 43* (*TARDBP*), *Fused in Sarcoma* (*FUS*), *P62* (*SQSTM1*), *Valosin-containing protein* (*VCP*) and *C9orf72* have been identified in familial forms of ALS (2–8). The existence of inherited ALS cases has provided excellent inroads towards unraveling the molecular pathology of the motor neuron diseases. Significantly, transgenic mice expressing mutant SOD1 have recapitulated the motor defects observed in ALS patients (9). Use of these mice has been

[†]These authors contributed equally to this work.

Received: May 8, 2015. **Revised:** July 29, 2015. **Accepted:** September 1, 2015

crucial in characterizing familial and sporadic ALS disease mechanisms (10). However, therapeutic efficacy in these animals has been poorly predictive of human efficacy. Therefore, it is crucial to create model systems associated with other mutations in ALS and analyze the resulting phenotypes.

ALS8 is a slowly progressive and late-onset dominant form of ALS first identified in a large Brazilian family (11). The family shows clinical heterogeneity with different clinical courses, such as late-onset spinal muscular atrophy (SMA), slowly progressive ALS and typical severe ALS with rapid progression (11,12). They are all found to have the same mutation (P56S) in the *VAPB* gene (11). In addition, recently, other rare mutations in the *VAPB* gene were also found to cause ALS (13,14).

Human *VAPB* is evolutionarily conserved, with homologs in numerous species (15), including yeast *scs2* and *Drosophila vap*. The Vap protein contains an amino (N)-terminal domain, called the major sperm protein (MSP) domain (16,17) and a transmembrane domain that anchors the protein in the endoplasmic reticulum (ER) (18). The N-terminal MSP domain of Vap is virtually identical in structure to the abundant MSP protein in C. elegans (19), where MSP functions as a secreted ligand (20,21). Indeed, the MSP domain of Vap is cleaved and secreted from neurons (22,23). The cleaved MSP acts as a ligand for growth cone guidance receptors expressed on muscle surfaces in C. elegans (23). Significantly, Vap proteins also have autonomous functions as they are ER-associated proteins. They have been shown to function in neurite extension (24), the development of the neuromuscular junctions (NMJs) (25), ER-to Golgi protein trafficking (26,27) and calcium homeostasis in the mitochondria (28). However, it is still not clear how these functions are relevant to the pathology in motor neuron disease.

Transgenic mice overexpressing P56S mutant human VAPB protein with neuron-specific and ubiquitous promoters have been generated (29–32). Although these mice have provided insights into the toxic property of the mutant proteins, only transgenic mice expressing P56S VAPB driven by Thy1.2 promoter showed motor behavior defects (30). Thus, the pathogenesis associated with the mutant VAPB protein remains unclear. Moreover, it has not been possible to undertake human pathological studies in ALS8/motor neuron disease associated with the mutant VAPB as the disease shows a late-onset ALS or SMA (average 50 years old) with a slowly progressive course (11,12).

Expressing the mutant proteins in the correct temporal and spatial expression patterns will help us dissect the mechanisms of cell-specific vulnerability and the effects of the pathological mutations. Here we report generation and characterization of *Vapb* knock-in mice replacing wild-type *Vapb* with the mutant (P56S) *Vapb* to faithfully create features of the human ALS8/SMA associated with P56S VAPB. Significantly, the *Vapb* knock-in mice exhibit late-onset motor behavior defects as observed in the patients associated with the P56S VAPB. The *Vapb* knock-in mice also display many cellular pathological features implicated in ALS, including accumulation of ubiquitinated proteins, ER stress and autophagic response before onset of obvious motor behavior defects. We propose that ER stress and autophagic response are key early pathogenic processes in the disease.

Results

Generation of $Vapb^{P56S}$ knock-in mice

To elucidate the pathological mechanism underlying motor neuron diseases associated with P56S mutant VAPB, we established knock-in mice replacing the wild-type *Vapb* gene ($Vapb^{WT}$) with the P56S mutant *Vapb* ($Vapb^{P56S}$) gene by homologous recombination (Fig. 1A and Supplementary Material, Fig. S1). Crosses between heterozygous mice carrying the P56S mutation produced wild-type ($Vapb^{WT}$), heterozygous ($Vapb^{WT/P56S}$) and homozygous ($Vapb^{P56S}$) offspring with a Mendelian ratio, in expected proportions (data not shown).

To determine if $Vapb^{P56S}$ gene in the targeted allele expresses *Vapb* transcript at comparable levels to those of $Vapb^{WT}$ gene in the wild-type allele, we performed quantitative real-time polymerase chain reaction (qRT-PCR) and measured the levels of *Vapb* transcripts in the brain of $Vapb^{WT}$, $Vapb^{WT/P56S}$ and $Vapb^{P56S}$ mice. The qRT-PCR in $Vapb^{WT/P56S}$ and $Vapb^{P56S}$ mice generate almost equivalent levels of products to those in $Vapb^{WT}$ mice (Fig. 1B. Average relative quantification (RQ) values, $Vapb^{WT/P56S}/Vapb^{WT} = 1.15$ and $Vapb^{P56S}/Vapb^{WT} = 1.56$, $N = 3$ mice, One way ANOVA, $P > 0.05$), suggesting that $Vapb^{P56S}$ gene in the targeted allele is transcribed at comparable levels to those of *Vapb* gene in the wild-type allele.

To determine the effects of P56S mutation on VAPB protein, we extracted the proteins from the spinal cord of WT and P56S knock-in mice with 1% NP-40 and collected detergent-soluble and insoluble fractions. Immunoblotting with VAPB antibody (33) shows a specific 26 kDa band corresponding to the full-length VAPB protein in the detergent-soluble fraction extracted from $Vapb^{WT}$ mice (Fig. 1C, lane 1, arrow). Compared with $Vapb^{WT}$ mice, the levels of VAPB protein are decreased in the detergent-soluble fraction of $Vapb^{WT/P56S}$ and, they are even further decreased in the $Vapb^{P56S}$ mice (Fig. 1C, lane 2, 3). In contrast, the amounts of truncated forms of VAPB protein are increased in the detergent-insoluble fraction of $Vapb^{WT/P56S}$ and $Vapb^{P56S}$ mice (Fig. 1C, lanes 4–6, arrows), indicating that the P56S mutation causes the VAPB protein to have altered physicochemical properties that lead to its detergent-insolubility. We observed decreased levels of full-length and increased levels of truncated VAPB protein in $Vapb^{P56S}$ mice, compared with those in $Vapb^{WT/P56S}$, suggesting the dose-dependent effect of $Vapb^{P56S}$ gene (compare lanes 2–3 and 5–6 in Fig. 1C). Interestingly, $VAPB^{P56S}$ protein migrates in SDS-PAGE with different electrophoretic properties, compared with $VAPB^{WT}$ protein (arrow lane 3′ in Fig. 1C), suggesting that P56S mutation causes post-translational modification of VAPB. In summary, P56S mutation causes detergent-insolubility of VAPB protein and possibly post-translational modification.

The P56S mutant *Vapb* knock-in mice show progressive defects in motor behavior in a dose-dependent manner

Patients with P56S mutant *VAPB* gene show neurological signs compatible with the diagnosis of lower motor neuron diseases or atypical form of ALS with slow progression (11,12). We found that both $Vapb^{WT/P56S}$ and $Vapb^{P56S}$ mice are born and develop normally and have a life span similar to $Vapb^{WT}$ mice. To determine whether the mice carrying the P56S mutation show defects in motor behaviors, we performed inverted grid and rotarod tests with a cohort of wild-type ($Vapb^{WT}$), heterozygous ($Vapb^{WT/P56S}$) and homozygous ($Vapb^{P56S}$) knock-in mice, tested from 7 to 15 months of age (Fig. 2). At 7 months of age, neither $Vapb^{WT/P56S}$ nor $Vapb^{P56S}$ mice show defects in the behavior tests compared with $Vapb^{WT}$ mice. Importantly, $Vapb^{WT/P56S}$ mice show mild defects in inverted grid at 11 months of age, and significant defects at 15 months of age. In contrast, $Vapb^{P56S}$ knock-in mice show severe and significant defects in inverted grid even at 11 months of age (Fig. 2A). Consistently, $Vapb^{WT/P56S}$ and $Vapb^{P56S}$ also showed age-dependent deficits in the rotarod test at 15 months (Fig. 2B).

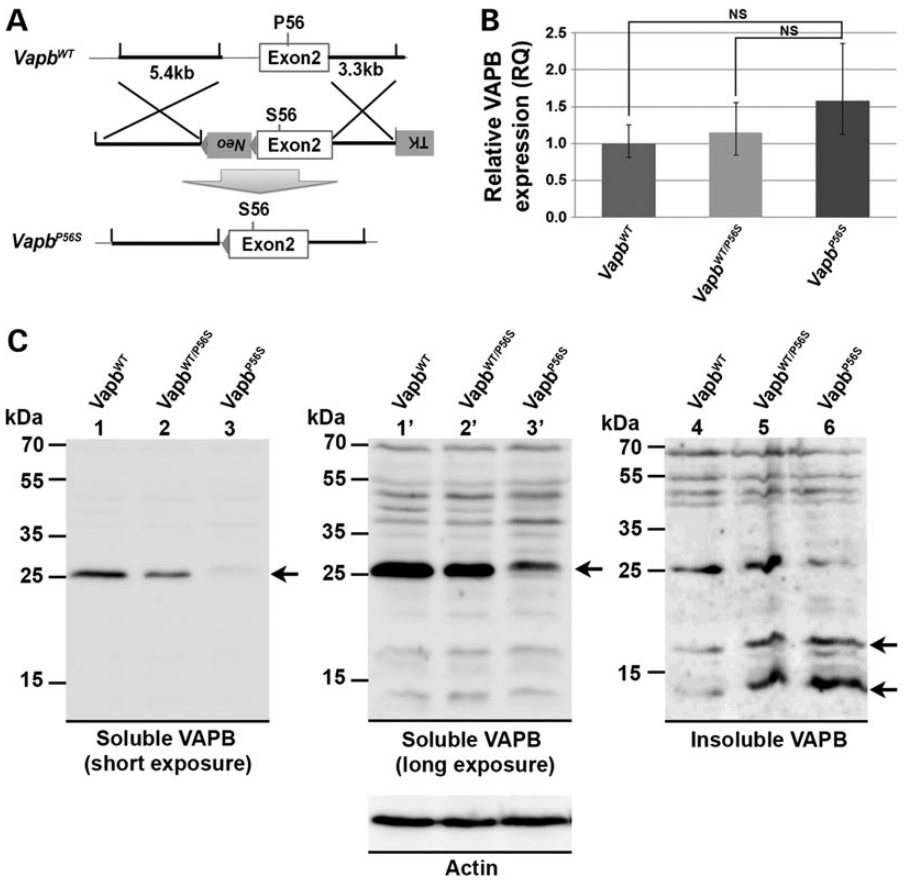

Figure 1. Generation of *Vapb* knock-in mice carrying the P56S mutation. (**A**) Schematic diagram showing gene targeting of mouse *Vapb* to insert P56S mutation. The *Vapb* targeting vector was designed to insert exon 2 carrying the P56S mutation and a PGK-Neomycin cassette flanked by LoxP. TK: Thymidine Kinase. (**B**) qRT-PCR of the mRNA extracted from the cerebrum of $Vapb^{WT}$, $Vapb^{WT/P56S}$ and $Vapb^{P56S}$ mice. Primers spanning exon 4 and exon 5 of *Vapb* gene were specifically designed to amplify *Vapb* cDNA, but not genomic *Vapb* (see method). The levels of qRT-PCR products in the $Vapb^{WT/P56S}$ and $Vapb^{P56S}$ mice are normalized with those in $Vapb^{WT}$. Error bars indicate the upper standard deviation (RQ max) and lower (RQ min). The differences between $Vapb^{WT}$, $Vapb^{WT/P56S}$ and $Vapb^{P56S}$ mice are not statistically significant (NS) ($N = 3$ mice, Oneway ANOVA, $P > 0.05$). (**C**) Immunoblot of 1% NP-40 soluble and insoluble fractions of proteins extracted from spinal cord of $Vapb^{WT}$, $Vapb^{WT/P56S}$ and $Vapb^{P56S}$ mice with VAPB antibody. The left and middle panels show immunoblots of the soluble fraction exposed in short and long periods. Arrows indicate full-length VAPB protein. VAPB quantity decreases in $Vapb^{WT/P56S}$ and $Vapb^{P56S}$extracts. The size of VAPB protein is increased in $Vapb^{P56S}$ (lanes 3, 3′) compared with $Vapb^{WT}$ (lanes 1, 1′). The right panel shows immunoblot of the insoluble fraction. Arrows show truncated forms of VAPB protein, observed in greater quantities in $Vapb^{WT/P56S}$ and $Vapb^{P56S}$ extracts. Actin was used as a loading control.

In contrast, no obvious differences were detected in body weight and Open-field tests among $Vapb^{WT}$, $Vapb^{WT/P56S}$ and $Vapb^{P56S}$ mice (Supplementary Material, Fig. S2). Hence, we have established that P56S knock-in mice exhibit slowly progressive defects in motor behavior analogous to those observed in human motor neuron disease associated with P56S VAPB.

The P56S mutant *Vapb* knock-in mice show mild and chronic neurogenic defects in muscle pathology

Analysis of muscle biopsies from ALS8 patients show defects consistent with a neurogenic pattern including groups of small angulated fibers (11,12). To examine if the ALS8 knock-in mice show neurogenic defects, we performed histological analysis of the soleus muscles of $Vapb^{WT}$ and $Vapb^{P56S}$ mice that were used in the behavior tests shown in Figure 2. We find that the muscle cross-sections of $Vapb^{WT}$ mice show groups of uniformly sized muscle fibers (Fig. 2C). In contrast, the muscle sections of the $Vapb^{P56S}$ mice show small group of atrophic cells (arrows in Fig. 2D and E, quantification in Fig. 2G). We also found an increased number of internal nuclei in muscle fibers of $Vapb^{P56S}$ (arrow heads in Fig. 2D and F, quantification in Fig. 2G). We, however, did not observe significant differences in the staining of muscle cross-sections of $Vapb^{WT}$ and $Vapb^{P56S}$ mice with an early denervation marker, non-specific esterase [(34), Supplementary Material, Fig. S4]. Hence, histochemical analysis of muscle cross-sections shows chronic and mild neurogenic atrophies in the $Vapb^{P56S}$ mice.

The P56S mutant *Vapb* knock-in mice show mild partial denervation of lower motor neurons

Mutant SOD1 transgenic mice and human ALS pathology have been characterized as dying back or slowly evolving distal to proximal axonal degeneration in the pathology (35–37). To determine if P56S mutant *Vapb* knock-in mice show denervation or morphological defects in the NMJs, we examined the morphology of the NMJs of $Vapb^{WT}$, $Vapb^{WT/P56S}$ and $Vapb^{P56S}$ mice. We performed immunostaining of soleus muscles of 16 months-old WT and ALS8 knock-in mice with a pre-synaptic (Synaptic vesicular protein 2, SV2) and post-synaptic marker [Acetylcholine receptors (AChRs) labeled with α-bungarotoxin] (Fig. 3A–C).

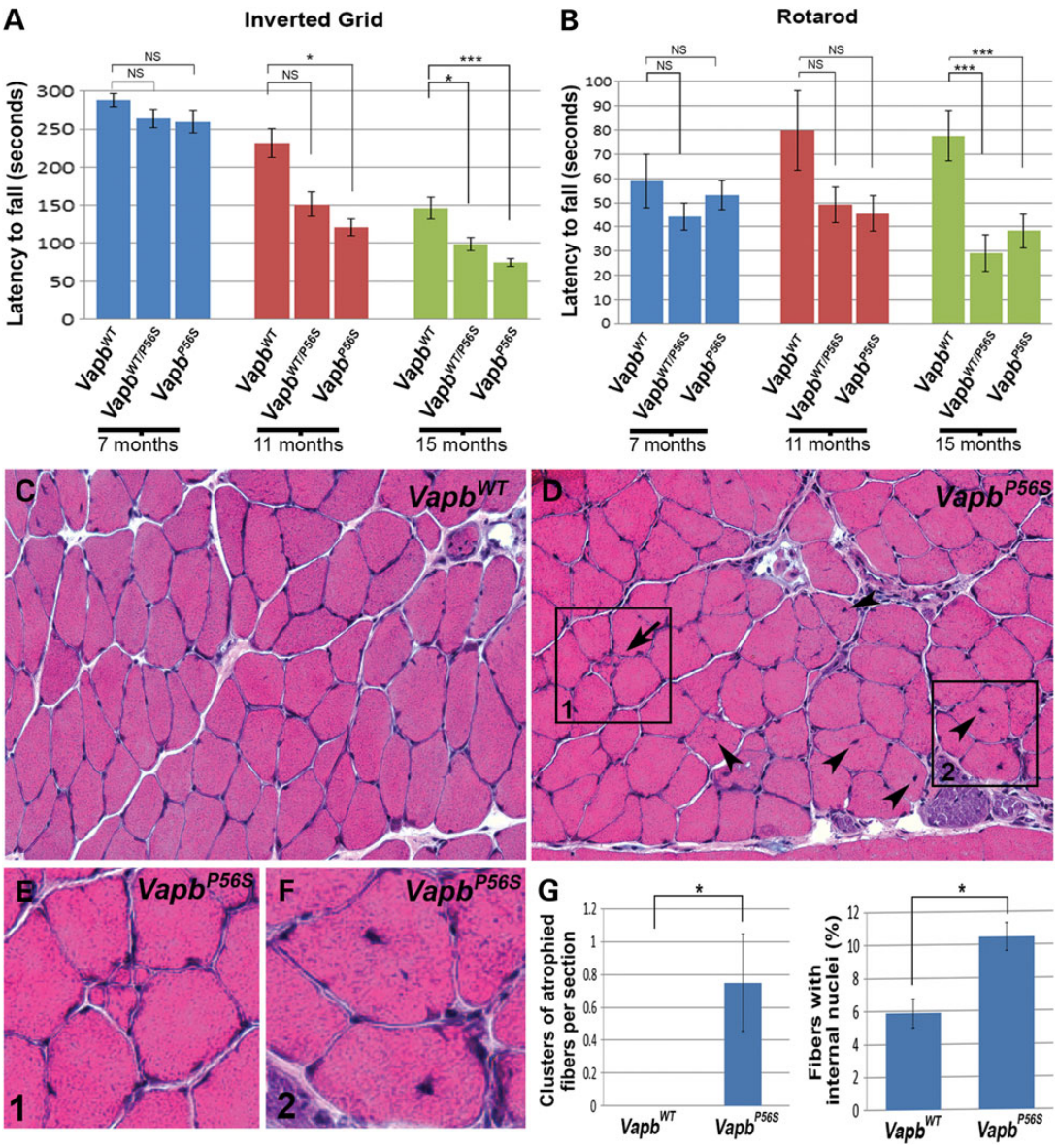

Figure 2. P56S mutation in the *Vapb* gene causes defects in motor behaviors and mild denervation changes in the muscle. (**A** and **B**) Inverted Grid (A) and Rotarod test (B) with a cohort of $Vapb^{WT}$ ($N = 7$), $Vapb^{WT/P56S}$ ($N = 9$) and $Vapb^{P56S}$ ($N = 8$) mice at 7, 11 and 15 months of age. The latencies to fall of the mice were recorded for both tests. The latency to fall by inverted grid test in $Vapb^{WT/P56S}$ and $Vapb^{P56S}$ is significantly lower in a dose-dependent manner compared with $Vapb^{WT}$ mice at 11 and 15 months of age. A significant decrease is notable in the latency to fall by rotarod test in $Vapb^{WT/P56S}$ and $Vapb^{P56S}$ compared with $Vapb^{WT}$ mice at 15 months of age. Data are presented as average ± SEM, $^{*}P < 0.05$, $^{***}P < 0.01$. (**C–G**) Hematoxylin and Eosin staining of soleus muscles of $Vapb^{WT}$ and $Vapb^{P56S}$ mice at 13 months of age. The muscle cross-sections of the wild-type mice show groups of uniformed size of muscle fibers (C). In contrast, the muscle sections of the *Vapb* knock-in mice show small group atrophies (D and E) and an increased number of fibers with internal nuclei (D and F). The number of group atrophies observed per section and the percentage of fibers with internal nuclei were quantified (G). Data are presented as average ± SEM. $N = 2$ for each genotype. $^{*}P < 0.05$.

Chronic denervation accompanying re-innervation of NMJs leads to increased fragmentation of the NMJs (38–40). Interestingly, we observed significant differences in the morphology of the NMJs between WT and P56S *Vapb* knock-in mice. The $Vapb^{WT}$ mice exhibit a typical pretzel-like appearance of post-synaptic area as observed in normal adult NMJs (Fig. 3A) (41). In contrast, $Vapb^{WT/P56S}$ and $Vapb^{P56S}$ mice show a fragmented appearance of post-synaptic areas (Fig. 3B and C). As shown in Figure 3D1, we found a significant increase in the total number of post-synaptic fragments per NMJ in $Vapb^{WT/P56S}$ and $Vapb^{P56S}$ mice (Number of fragments: $vapb^{WT} = 8.1 \pm 0.6$, $Vapb^{WT/P56S} = 12.9 \pm 1.0$, $Vapb^{P56S} = 17.9 \pm 1.3$, $^{***}P < 0.01$ for each pair), suggesting chronic denervation accompanied with re-innervation in the $Vapb^{WT/P56S}$ and $Vapb^{P56S}$ mice. We also examined other indications of denervation (Supplementary Material, Fig. S5, see Materials and Methods), including distribution of the post-synaptic area as defined by AChR staining (α-bungarotoxin labeling) and its coverage with pre-synaptic markers as defined by SV2 (Fig. 3D2) and the number of faintly clustered or ectopic AChR staining clusters (Fig. 3D3 and Fig. 3D4) (42). We observed a tendency towards an increased number of uncovered postsynapses (AChR) (Fig. 3D2) and ectopic AChR (Fig. 3D4) in the $Vapb^{WT/P56S}$ and $Vapb^{P56S}$ mice at 16 months of age. Hence, the $Vapb^{WT/P56S}$ and $Vapb^{P56S}$ mice show chronic denervation, although the denervation is likely to be very mild.

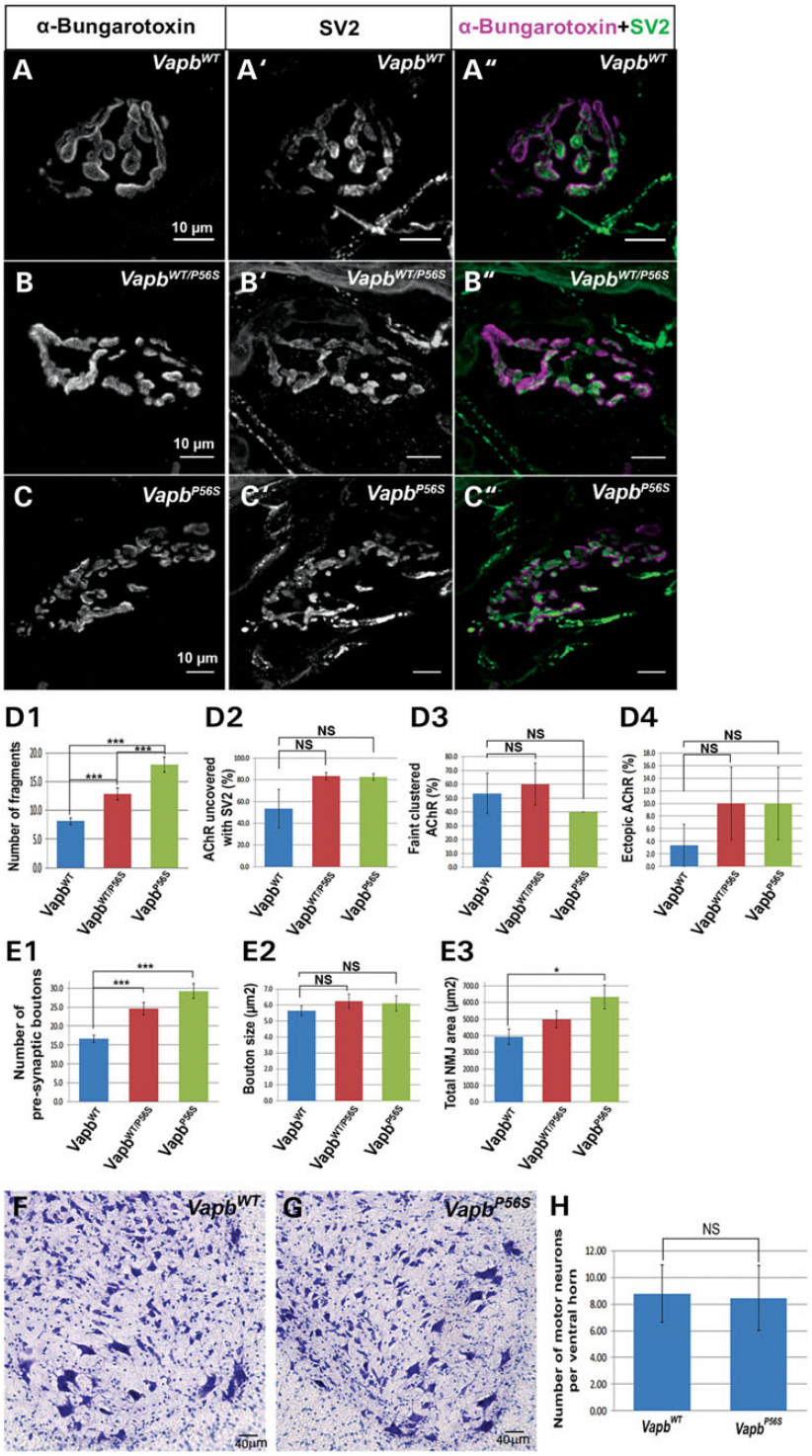

Figure 3. The P56S mutant *Vapb* knock-in mice show mild partial denervation of lower motor neurons and morphological defects in the NMJs. (**A–C**) Representative pictures of NMJs observed on parallel myofibrils of soleus for $Vapb^{WT}$(A–A″), $Vapb^{WT/P56S}$ (B–B″) and $Vapb^{P56S}$ mice (C–C″). Staining with α-bungarotoxin and SV2 antibody. The NMJ in $Vapb^{WT}$ displays a compact and pretzel-like appearance (A). NMJs in $Vapb^{WT/P56S}$ and $Vapb^{P56S}$ mice are both highly fragmented, and present an increased endplate area with numerous synaptic boutons (B and C). (**D**) Quantification of NMJs innervation phenotypes showing the number of post-synaptic fragments (D1), the fraction of NMJs showing AChR uncovered with SV2 (D2), faint clustered AChR (D3) and ectopic AChR (D4). See the criteria in materials and methods and Supplementary Material, Figure S5. Compared with $Vapb^{WT}$, $Vapb^{WT/P56S}$ and $Vapb^{P56S}$ mice show a significantly increased number of post-synaptic fragments (D1). Three female mice for each genotype and 30 NMJs of each mice were analyzed. (**E**) Quantification of NMJs morphology showing the number of pre-synaptic boutons (E1), the average bouton size (E2) and the total endplate area (E3). The number of boutons is significantly increased in $Vapb^{WT/P56S}$ and $Vapb^{P56S}$ mice compared with $Vapb^{WT}$ (E1). The total endplate area increases significantly in homozygous $Vapb^{P56S}$ mice (E3). Three female mice for each genotype and 30 NMJs of each mice were analyzed. Data are presented as average ± SEM, $^{*}P < 0.05$, $^{***}P < 0.01$. (**F–H**) Histochemical analysis of spinal cord sections. Motor neurons in the ventral horn of the spinal cord from $Vapb^{WT}$ (F) and $Vapb^{P56S}$ (G) mice were stained with Cresyl Violet. The numbers of motor neurons in the sections were quantified (H, 10 sections/animal, $N = 3$ for each genotype). Decreased numbers of the motor neuron was not observed in $Vapb^{P56S}$ mice.

To determine the loss of motor neurons and defects in cell bodies, we performed Nissl staining (Fig. 3F and G) and quantification analysis of numbers of large motor neurons in the spinal cord (Fig. 3H). We did not observe a difference between the number of the motor neurons in the spinal cord of $Vapb^{WT}$ and $Vapb^{P56S}$ mice. Taken altogether, the data suggest that P56S mutation causes neurogenic defects, resulting in partial chronic denervation with vulnerable defects in the NMJs.

The P56S mutant *Vapb* knock-in mice show morphological changes of the synaptic boutons in the NMJs

Drosophila Vap (*dvap*) is the structural homolog of human VAPB and regulates synaptic remodeling by affecting the size and number of boutons (synaptic varicosities) at NMJs (25,43). To determine the effect of P56S mutation on bouton number and morphology in adult mice, we performed analysis of the NMJs in the soleus muscles from 16-month old $Vapb^{WT}$, $Vapb^{WT/P56S}$ and $Vapb^{P56S}$ mice (Fig. 3). We found a significant increase in the number of pre-synaptic boutons in $Vapb^{WT/P56S}$ and $Vapb^{P56S}$ when compared with $Vapb^{WT}$ mice (Fig. 3E1, Number of boutons: $vapb^{WT} = 16.6 \pm 1.0$, $Vapb^{WT/P56S} = 24.6 \pm 1.6$, $Vapb^{P56S} = 29.3 \pm 1.9$, $^{***}P < 0.01$ for both pairs $Vapb^{WT/P56S}/Vapb^{WT}$ and $Vapb^{P56S}/Vapb^{WT}$).

In contrast, the size of synaptic boutons is not significantly different among $Vapb^{WT}$, $Vapb^{WT/P56S}$ and $Vapb^{P56S}$ mice (Fig. 3E2). We also observed an increased endplate area in the $Vapb^{WT/P56S}$ and, significantly, in the $Vapb^{P56S}$ mice in a gene dosage-dependent manner (Fig. 3E3, Total endplate area: $vapb^{WT} = 393.7 \pm 46.4\ \mu m^2$, $Vapb^{WT/P56S} = 498.4 \pm 50.7\ \mu m^2$, $Vapb^{P56S} = 634.3 \pm 71.9\ \mu m^2$, $^{*}P < 0.05$ for $Vapb^{P56S}/Vapb^{WT}$). Of note, *Vapb* null mutant mice have been shown to exhibit the same morphology of NMJs as $Vapb^{WT}$ mice even at 18 months of age (13). Taken together, the data suggests that P56S mutation causes morphological changes of the synaptic boutons in the NMJs of adult mice. Similar changes are also observed in flies expressing ALS8 mutant Vap (44).

VAPB protein is predominantly expressed in lower motor neurons

Human ALS8 patients affected with the P56S mutant *VAPB* gene show weakness and muscle atrophy associated with defects in lower motor neurons rather than upper motor neurons (12). To determine whether the distribution of VAPB protein might contribute to the selective vulnerability of motor neurons in ALS8, we examined expression of VAPB in the CNS and spinal cord in mice. To assess the specificity of VAPB antibody (33), we performed immunostaining of wild-type and mutant mice carrying a gene trap mutation in the *Vapb* locus ($Vapb^{GT}$). The $Vapb^{GT}$ mice were generated from embryonic stem (ES) cells carrying a gene-trapping vector inserted into the *Vapb* locus (Supplementary Material, Fig. S3A) (45,46). We confirmed that $Vapb^{GT}$ mice are almost *Vapb null* with immunofluorescence and western blotting using VAPB antibody (Fig. 4A and B and Supplementary Material, Fig. S3B). Immunolabeling with VAPB antibody in WT and heterozygous $Vapb^{+/GT}$ shows that VAPB protein is expressed predominantly in motor neurons (Fig. 4C and Data not shown), but not in sensory or other populations of neurons (Fig. 4D) within the spinal cord. VAPB was predominantly expressed in neuronal cell bodies and their dendrites (Fig. 4A and C), whereas VAPB shows little or no expression in glia cells (Fig. 4C). VAPB is also highly expressed in the motor neurons of the caudal brainstem (Fig. 4E), which is co-labeled with Choline Acetyltransferase antibody (data not shown). In contrast, VAPB is barely expressed in the cerebellum (Fig. 4F), the cerebrum (including cortical motor neurons labeled with CITP2) (Fig. 4G) and the hippocampus (Fig. 4H). In summary, the data indicate that VAPB is highly expressed in the lower motor neurons, which are the most vulnerable to dysfunction or degeneration in ALS8 or SMA.

The P56S mutation causes VAPB protein to be mislocalized into cytoplasmic inclusions

We, and others, have shown that the P56S mutation causes VAPB protein to be mislocalized into cytoplasmic inclusions when the mutant protein is overexpressed in flies and mice (22,29,30). However, the overexpression of proteins might cause or enhance defects in protein homeostasis, leading to the accumulation of the mutant protein. To determine the localization of P56S mutant VAPB protein when expressed at physiological levels, we performed immunostaining of motor neurons in the spinal cord of $Vapb^{WT}$, $Vapb^{WT/P56S}$ and $Vapb^{P56S}$ mice with VAPB antibody (33) at 6 months of age before defects in motor behaviors were observed (Fig. 2). As shown in Figure 5, $Vapb^{P56S}$ mice exhibit a significant difference in the localization of VAPB protein compared with $Vapb^{WT}$ mice. In the motor neurons of the spinal cord and brainstem of $Vapb^{WT}$ mice, VAPB protein distributes diffusely in the cytoplasm (Fig. 5A). In contrast, VAPB protein accumulates into cytoplasmic inclusions in the $Vapb^{WT/P56S}$ mice. Interestingly, $Vapb^{P56S}$ mice show more widespread inclusions with no diffuse cytoplasmic distribution as observed in $Vapb^{WT}$ mice (Fig. 5C). We found that $Vapb^{P56S}$ mice show an increased number of cells presenting inclusions compared with $Vapb^{WT/P56S}$ (Fig. 5D, $Vapb^{WT} = 0\%$ of cells with VAPB immunopositive inclusions, $Vapb^{WT/P56S} = 70.9\%$ ±9.3 s.e.m, and $Vapb^{P56S} = 100\%$, ANOVA then post-hoc Multiple student *t*-test, $P < 0.01$, $N = 3$), suggesting dose-dependent defects caused by $Vapb^{P56S}$ gene. As we observe that VAPB is highly expressed in lower motor neurons, but not in other types of neurons, we do not observe VAPB inclusions in the other types of neurons in $Vapb^{WT/P56S}$ and $Vapb^{P56S}$ mice (data not shown). Taken together, the data show that VAPB protein accumulates into cytoplasmic inclusions selectively in lower motor neurons before the onset of behavior defects in $Vapb^{P56S}$ knock-in mice.

The P56S mutant VAPB is translocated from the ER to the autophagosome

We, and others, have shown that $VAPB^{WT}$ is localized in the ER (22,47). To determine the intracellular location of $VAPB^{P56S}$ accumulations, we performed immunostaining of spinal cord sections from $Vapb^{WT}$ and $Vapb^{P56S}$ mice with anti-VAPB antibody and ER markers specific anti-Calreticulin (48) and KDEL antibodies (49). Consistent with the previous observations that VAPB is localized in the ER (47), $VAPB^{WT}$ colocalized with the ER markers, KDEL and Calreticulin in $Vapb^{WT}$ mice (Fig. 6A, C and Data not shown). Significantly, in $Vapb^{P56S}$ mice, the mutant $VAPB^{P56S}$ is excluded from the ER as it does not co-localize with KDEL and Calreticulin (Fig. 6B, D and Data not shown), suggesting that the mutant $VAPB^{P56S}$ is mislocalized and absent from the ER.

Ubiquitin immunoreactive inclusions in lower motor neurons represent a characteristic pathological feature of ALS (50). Importantly, the mutant $VAPB^{P56S}$ has been shown to be ubiquitinated and accumulated with ubiquitinated proteins in flies and mice when the mutant protein is overexpressed (22,29,30). However, $VAPB^{P56S}$ protein is barely extractable in non-ionic detergent and sequence detection system (SDS) buffer. Therefore, we

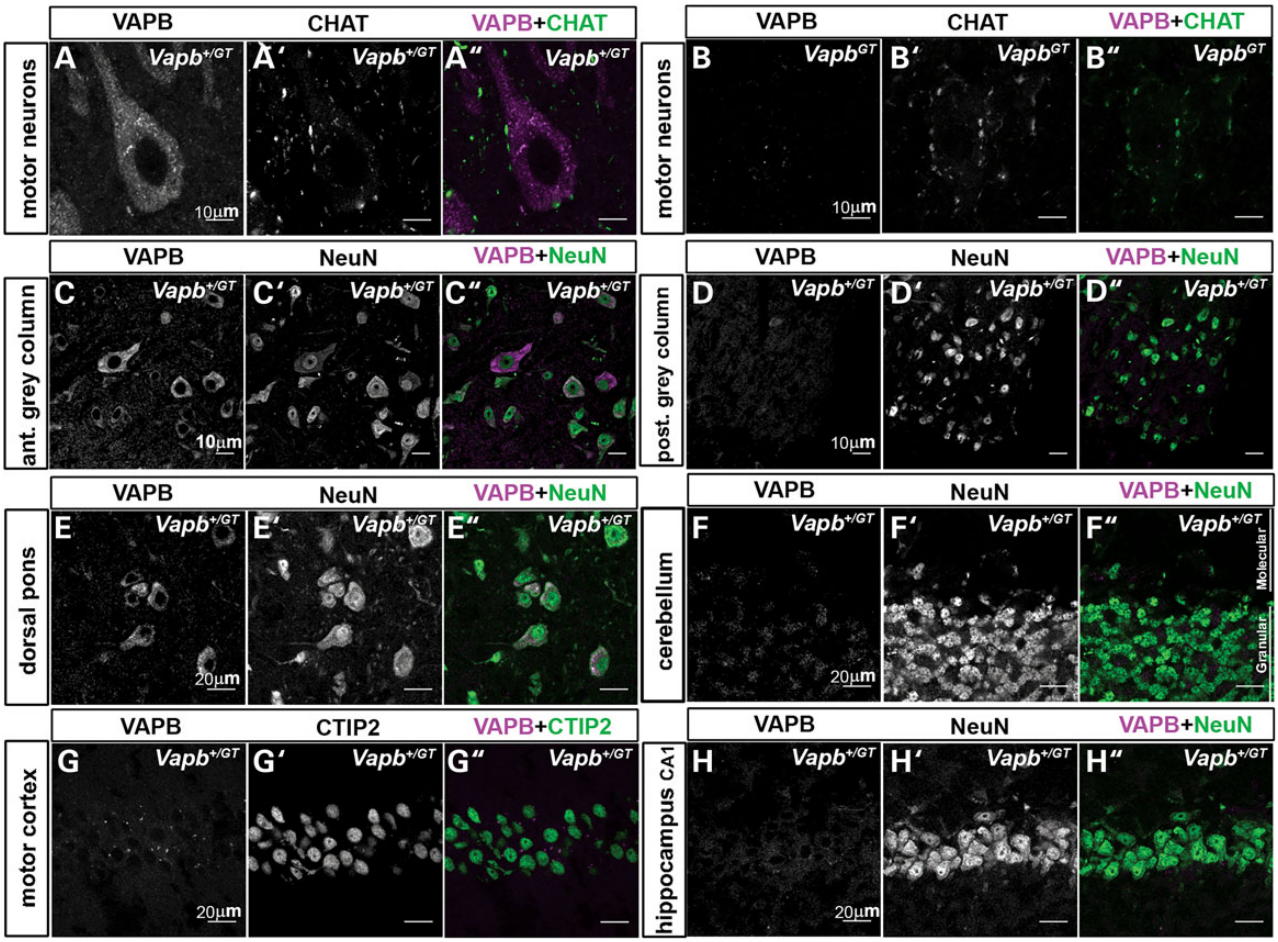

Figure 4. VAPB protein is predominantly expressed in lower motor neurons. (**A** and **B**) Staining of motor neurons in the spinal cord of $Vapb^{+/GT}$ (A–A″) and $Vapb^{GT/GT}$ (B–B″) with VAPB (A and B) and Choline Acetyltransferase (CHAT) (A′, B′) antibodies showing specificity of VAPB antibody against $VAPB^{WT}$ protein. (**C** and **D**) Staining of anterior gray column (C) and posterior gray column (D) in the spinal cord of $Vapb^{+/GT}$ mice with VAPB (C and D) and NeuN antibodies (C′ and D′). VAPB is predominantly expressed in the NeuN positive motor neurons located in anterior gray column (C), but not in the neurons of the posterior gray column (D). (**E–H**) Staining of dorsal pons (E), cerebellum (F), motor cortex (G) and CA1 of hippocampus (H) with VAPB antibody (E–H), NeuN antibody (E′, F′ and H′) and CTIP2 (G′). VAPB is expressed in NeuN positive neurons in the dorsal pons (E–E″), but barely expressed in the cerebellum (F–F″) and neurons in the motor cortex (G–G″) and hippocampus (H–H″).

examined if $VAPB^{P56S}$ accumulates into ubiquitinated inclusions in the $Vapb^{P56S}$ knock-in mice. We performed immunostaining of motor neurons of $Vapb^{WT}$ and $Vapb^{P56S}$ mice with VAPB and Ubiquitin (FK1) antibodies at 9 months of age. In $Vapb^{WT}$ mice, ubiquitinated proteins labeled by the antibody are barely expressed in the motor neurons (Fig. 6E′, E″), whereas ubiquitinated proteins accumulate in cytoplasmic inclusions in the $Vapb^{P56S}$ mice (Fig. 6F′, F″). Importantly, the mutant $VAPB^{P56S}$ is significantly colocalized with poly-ubiquitinated proteins (Fig. 6F″), suggesting that $VAPB^{P56S}$ might be ubiquitinated or recruit ubiquitinated proteins.

Ubiquitinated proteins are processed by the proteasome system or degraded by the autophagic machinery or lysosome (51). To determine if mislocalized $VAPB^{P56S}$ is recruited into the autophagosome, we performed immunostaining of $Vapb^{WT}$ and $Vapb^{P56S}$ mice with early autophagy markers, P62/SQSTM1 (52) and LC3 (53). LC3 is diffusely expressed at low levels in $Vapb^{WT}$ mice (Fig. 6G′, G″). In contrast, LC3 is upregulated in the cytoplasm and accumulates in inclusions in the $Vapb^{P56S}$ mice (Fig. 6H′, H″). Similarly, P62 is upregulated in $Vapb^{P56S}$ mice, compared with $Vapb^{WT}$ mice (Compare Fig. 6I′ and 6J′). Importantly, $VAPB^{P56S}$ protein, P62 and LC3, the early autophagosome markers, are significantly colocalized in the cytoplasmic inclusions in $Vapb^{P56S}$ mice (Fig. 6H–H″ and 6J–J″).

To determine if autophagy markers are upregulated in the heterozygous $Vapb^{WT/P56S}$ mice, we performed immunoblotting of protein extracted with 18–24 months-old $Vapb^{WT}$ and $Vapb^{WT/P56S}$ mice with P62 antibody. We found that the levels of P62 in $Vapb^{WT/P56S}$ mice are four times higher compared with $Vapb^{WT}$ mice (Fig. 6K and L), suggesting an increased autophagic response caused by P56S mutant VAPB. Hence, the data indicate that the P56S mutation causes VAPB protein to be mislocalized from ER to autophagosome and results in the autophagic response.

The P56S mutant VAPB causes ER stress

VAPB is localized in the ER and required for ER protein homeostasis (54,55). We observed that P56S mutant VAPB is barely localized in the ER (Fig. 6A–D), suggesting that P56S mutation might cause loss of VAPB function in the ER. We showed that loss of Vap induces ER stress in flies (55). To examine if the $Vapb^{P56S}$ knock-in mice exhibit ER stress, we stained spinal cords of $Vapb^{WT}$ and $Vapb^{P56S}$ mice with ER stress markers, PDI (56) and GRP78/BiP (57) at 6 months and 9 months of age. PDI is expressed at low

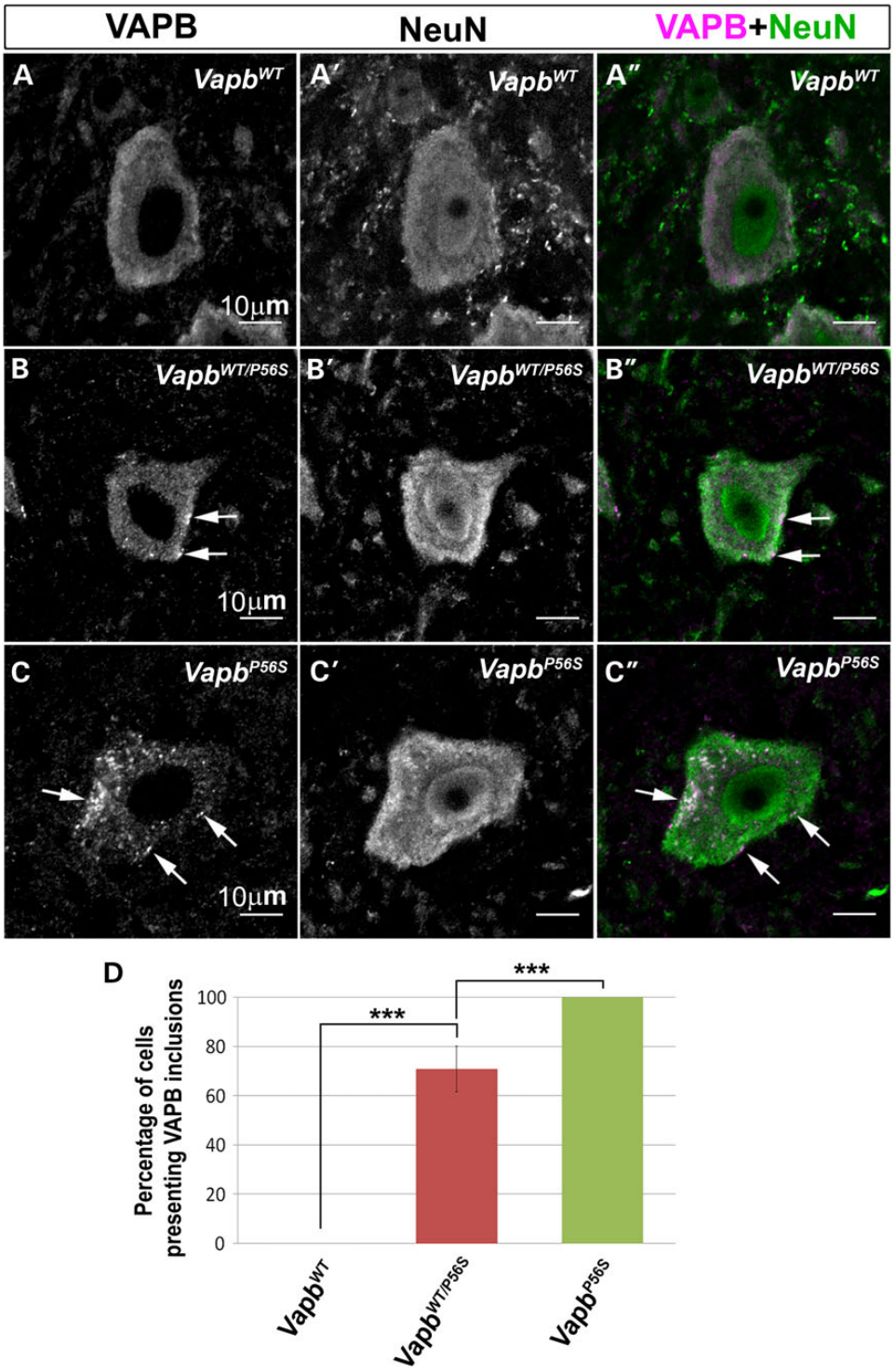

Figure 5. The P56S mutation causes VAPB protein to be mislocalized into cytoplasmic inclusions. (**A–C**) Staining of 6 months-old *Vapb*^{WT} (A), *Vapb*$^{WT/P56S}$ (B) and *Vapb*^{P56S} (C) mice with anti-VAPB (A–C) and anti-NeuN (A′–C′) antibodies. VAPB is diffusely distributed in the cytoplasm of *Vapb*^{WT} mice (A), whereas VAPB accumulates as punctae in the cytoplasm of motor neurons (B, arrows) of *Vapb*$^{WT/P56S}$ mice. VAPB-positive inclusions are increased in number and distributed widely in *Vapb*^{P56S} mice, compared with *Vapb*$^{WT/P56S}$ (C, arrows). (**D**) Quantification of the fraction of motor neurons presenting VAPB inclusions in *Vapb*^{WT}, *Vapb*$^{WT/P56S}$ and *Vapb*^{P56S} mice. Error bars represent average ± SEM ($N = 3$, ANOVA then post-hoc Multiple student *t*-test, $^{***}P < 0.01$).

levels in *Vapb*^{WT} mice (Fig. 7E), whereas PDI is significantly upregulated in the *Vapb*^{P56S} mice (Fig. 7F). We also find that *Vapb*^{P56S} mice show significant upregulation of BiP expression in the motor neurons at the age of 9 months (Fig. 7A–D), suggesting that P56S mutant VAPB causes ER stress in *Vapb*^{P56S} mice. The ER stress in *Vapb*^{P56S} mice is likely to be age dependent, as we do not observe upregulation of BiP in *Vapb*^{P56S} mice at 6 months of age (data not shown).

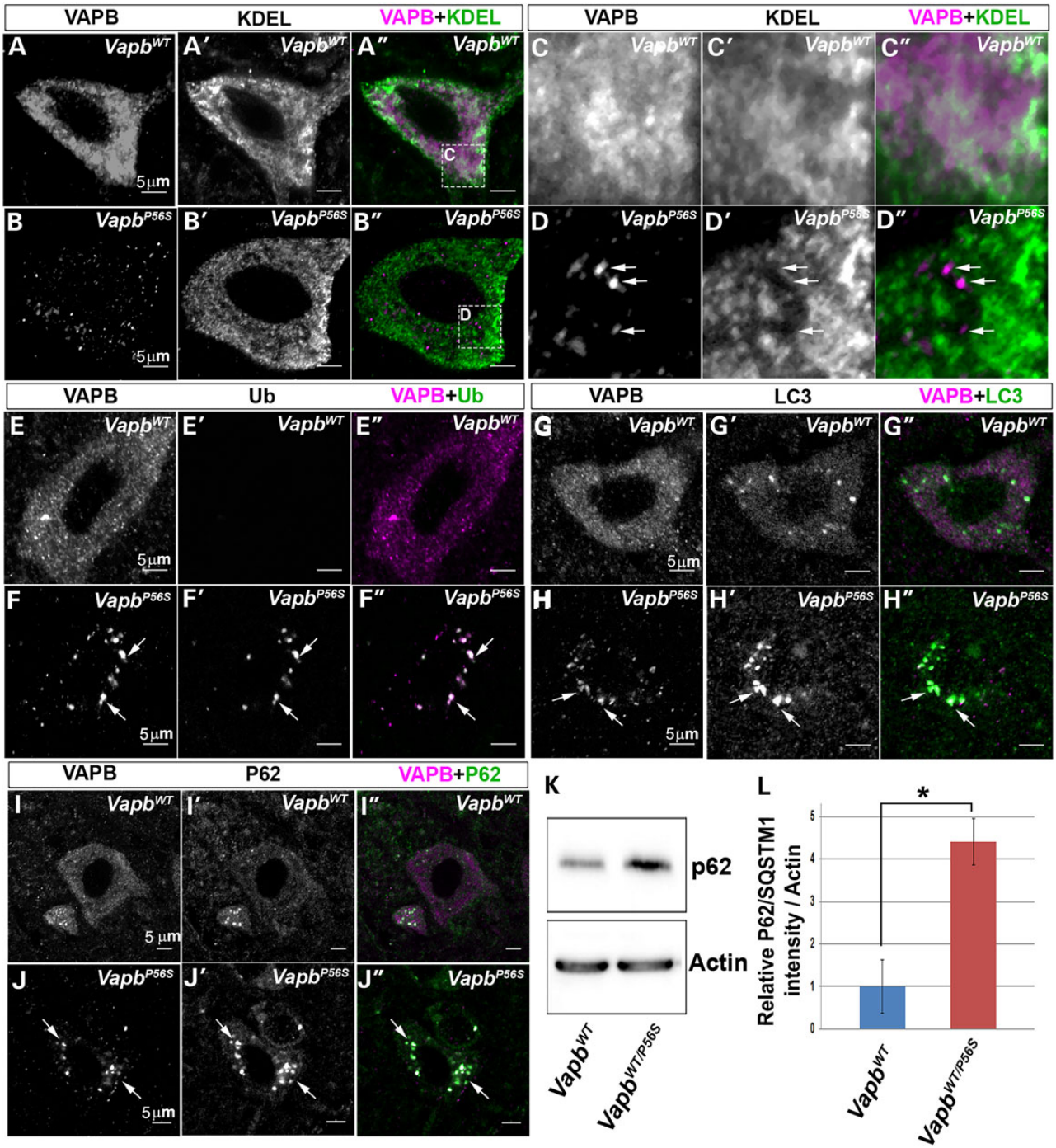

Figure 6. The P56S mutation causes VAPB protein mislocalization from the ER to the autophagosome. (**A–D**) Staining of motor neurons in the spinal cord of $Vapb^{WT}$ (A–A″, C–C″) and $Vapb^{P56S}$ mice (B–B″, D-D″) with anti-VAPB (A–D) and anti-KDEL (A′–D′) at 8 months of age. (C) and (D) show higher magnification of (A) and (B), respectively. $VAPB^{WT}$ is colocalized with KDEL, the ER marker (C–C″), whereas $VAPB^{P56S}$ does not colocalize with the ER marker (arrows in D–D″). (**E** and **F**) Staining of motor neurons in the spinal cord of the $Vapb^{WT}$ (E–E′) and $Vapb^{P56S}$ mice (F–F″) with anti-VAPB (E and F) and anti-Ubiquitin (E′, F′) at 8 months of age. No significant Ubiquitin positive signals were observed in $Vapb^{WT}$ mice (E′), whereas Ubiquitin positive inclusions were observed in the cytoplasm of motor neurons in $Vapb^{P56S}$ mice (F′). VAPB-positive inclusions are almost completely overlapped with Ubiquitinated inclusions (F–F″). (**G** and **H**) Staining of motor neurons in the spinal cord of 9 months-old $Vapb^{WT}$ (G) and $Vapb^{P56S}$ (H) mice with antibodies against VAPB (G and H) and LC3 (G′ and H′), an autophagy marker. LC3 accumulated into cytoplasmic inclusions in the mutant mice (H′) and colocalizes with VAPB (H). LC3 is also upregulated in $Vapb^{P56S}$ (H′), compared with $Vapb^{WT}$ (G′). (**I** and **J**) Staining of motor neurons in the spinal cord of 8 months-old $Vapb^{WT}$ (I) and $Vapb^{P56S}$ (J) mice with antibodies against VAPB (I and J) and P62/SQSTM (I′ and J′), another autophagy marker. Almost all VAPB-positive inclusions are P62 positive (J and J′). Note that the levels of P62 are increased in $Vapb^{P56S}$ (J′), compared with $Vapb^{WT}$ (I′). (**K** and **L**) Immunoblots of proteins extracted from spinal cord of 18 months-old $Vapb^{WT}$ and $Vapb^{WT/P56S}$ using anti-P62 and anti-Actin. The levels of P62 expression are quantified in (L). Intensities were normalized with Actin then a ratio was calculated using $Vapb^{WT}$ as a reference so that the relative $Vapb^{WT}$ intensity is set to 1. Error bars represent SEM of the intensities. The expression levels of P62 protein are significantly increased in $Vapb^{WT/P56S}$, compared with $Vapb^{WT}$ ($N = 3$, Student t-test, $^*P < 0.05$).

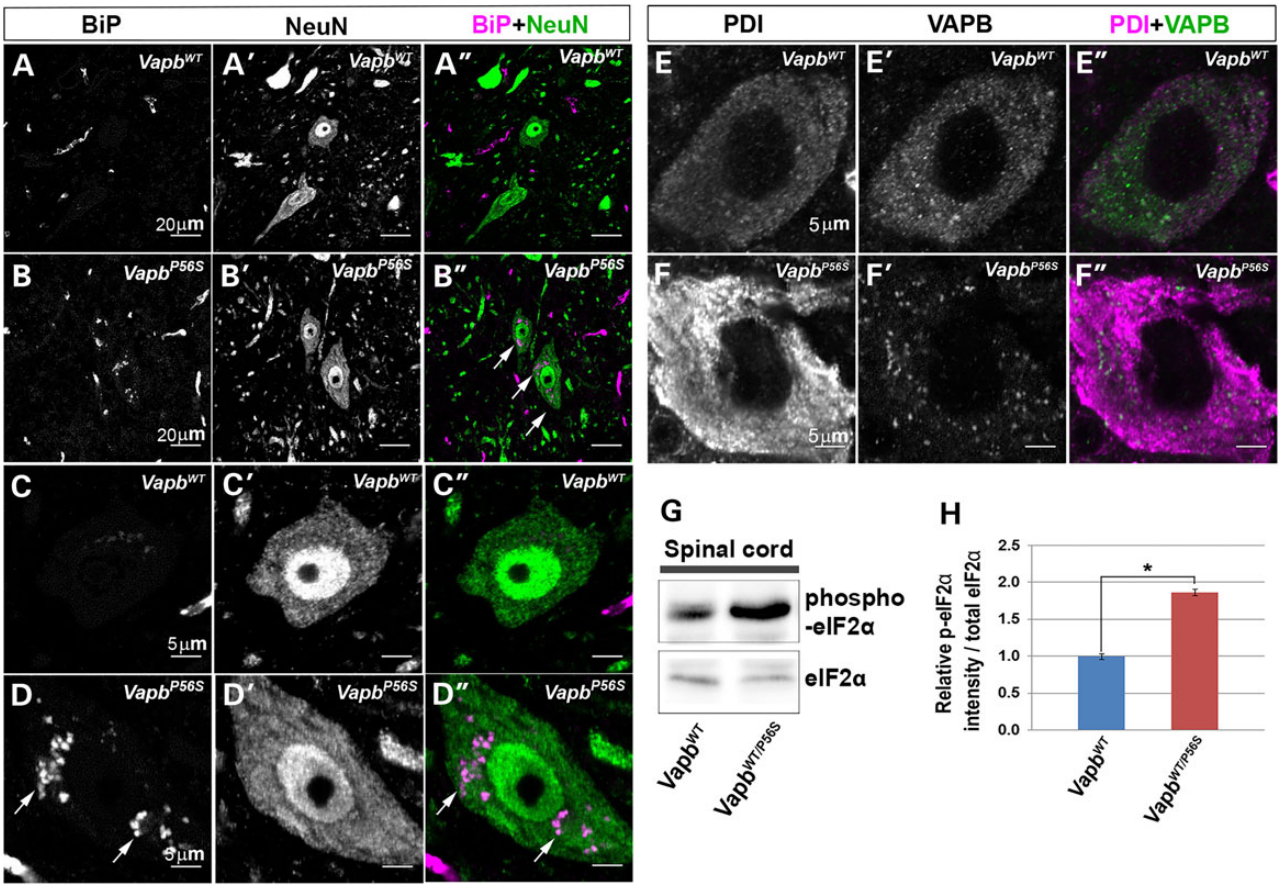

Figure 7. The P56S mutant VAPB causes ER stress. (**A–D**) Staining of spinal cord motor neurons of 10 months-old *Vapb*^{WT} and *Vapb*^{P56S} mice with anti-BiP, an ER stress marker (A and D) and NeuN (A′, D′). (C and D) High magnification images of (A) and (B). The expression levels of BiP are upregulated in *Vapb*^{P56S} mice (B and D), but not in the *Vapb*^{WT} (A and C). (**E** and **F**) Staining of spinal cord motor neurons of 10 months-old *Vapb*^{WT} and *Vapb*^{P56S} mice with anti-PDI, another ER stress marker (E and F) and VAPB (E′ and F′). PDI expression is significantly upregulated in *Vapb*^{P56S} mice (F) compared with *Vapb*^{WT} mice (E). (**G** and **H**) Immunoblots of proteins extracted from spinal cord of *Vapb*^{WT} and *Vapb*$^{WT/P56S}$ 18 months-old mice with anti-phospho-eIF2α and anti-eIF2α. (H) Quantification of phosphorylation of eIF2α. p-eIF2α intensities were normalized with total eIF2α. A ratio was calculated using *Vapb*^{WT} as a reference so that the relative *Vapb*^{WT} intensity is set to 1. Error bars represent SEM of the intensities. The levels of p-eIF2α are significantly increased in *Vapb*$^{WT/P56S}$ compared with those in *Vapb*^{WT} ($N = 3$ for each genotype, Student *t*-test, $^*P < 0.05$).

We find that *Vapb*$^{WT/P56S}$ mice do not show BiP upregulation at 9 months of age, compared with *Vapb*^{P56} mice (data not shown). To determine if heterozygous *Vapb*$^{WT/P56S}$ mice show ER stress when aging, we performed immunoblotting of *Vapb*^{WT} and *Vapb*$^{WT/P56S}$ mice with another ER stress marker, phosphorylated eIF2α (p-eIF2α) (58). As shown in Figure 7G and H, the levels of p-eIF2α, normalized by total eIF2α, in *Vapb*$^{WT/P56S}$ mice are increased by 86% compared with those in *Vapb*^{WT} mice at 18–25 months of age. Hence, *Vapb*$^{WT/P56S}$ mice show ER stress similarly as observed in *Vapb*^{P56S} mice, though the ER stress in *Vapb*$^{WT/P56S}$ is much milder than in *Vapb*^{P56S} mice. The ER stress in *Vapb*^{P56S} mice is likely to be predominantly induced in the lower motor neurons, as we do not observe upregulation of p-eIF2α in the brain of *Vapb*^{P56S} mice (Supplementary Material, Fig. S6). In addition, the ER stress seems to be partially activated or compensated in *Vapb*^{P56S} mice. We performed qRT-PCR of mRNA extracted from 13 months-old *Vapb*^{WT} and *Vap* ^{P56S} mice to determine the upregulation of genes associated with the ER stress apoptosis including ATF4, ATF6 and CHOP (56,59) (Supplementary Material, Fig. S7). We did not observe significant differences of the levels of the expression in the *Vapb*^{WT} and *Vapb*^{P56S} mice.

Discussion

Previous studies have shown that transgenic mice overexpressing ALS mutant VAPB proteins with neuron-specific and ubiquitous promoters fail to show defects in motor behaviors (29,31,32,43). Among these ALS8 *Vapb* transgenic mice, only transgenic mice expressing ALS mutant Vap under the Thy1.2 promoter show motor behavior defects in aged mice. In this study, we have shown that the *Vapb*^{P56S} knock-in mice develop a slowly progressive motor neuron disease reminiscent of ALS8. Muscle weakness shown by grip test is apparent at 11 months of age. Patients associated with P56S mutation also display clinical signs associated with defects in lower motor neurons, with an average age of around 50 at onset (11). We do not observe loss of body weight in the *Vapb*$^{WT/P56S}$ and *Vapb*^{P56S} knock-in mice. It is possible that body weight loss will not appear within the short life span of a mouse. Interestingly, these mice show cellular pathological defects specifically in motor neurons. The mutant mice demonstrate accumulation of ubiquitinated protein, induction of ER stress and autophagic response before showing motor deficits. Hence, having succeeded in developing a mouse model that invokes the correct temporal and spatial expression of the

disease-causing mutation, some of the pathogenic questions that are specific to motor neuron diseases associated with P56S VAPB can begin to be addressed.

We propose that P56S mutation causes hypomorphic and dominant negative defects in the ALS8 knock-in mice. Rescue studies with the ALS8 mutant Vap in zebrafish suggests that the defects caused by the ALS8 mutant protein are hypomorphic (13,55). In the ALS8 knock-in mice, P56S mutant VAPB is mislocalized and absent in the ER, indicating that ALS8 mutation causes VAPB protein to be less active in the ER, resulting in the ER stress. However, *Vapb* null mice show rather mild phenotypes compared with the ALS8 knock-in mice (13). Previous studies showed that the Vap^{ALS8} protein causes dominant defects when the mutant protein is overexpressed in flies and mice (30,43,44), suggesting that VAPB might also act as a dominant negative against WT VAPB or VAPA proteins in ALS8 knock-in mice. Significantly, impaired VAPB function may contribute to the pathogenesis of familial and sporadic forms of ALS. VAPB levels decrease concomitantly with the disease's progression in the SOD1 mouse model (47), and sporadic ALS patients have been reported to have decreased levels of the VAPB protein (47,60). Defects in ER protein homeostasis and ER stress are also commonly observed in ALS patients (61–63), suggesting that loss of VAPB function in the ER might cause common pathology in ALS.

Interestingly, ALS8 mutation might also cause gain of function in certain situations in the ALS8 knock-in mice. We observed that the ALS8 knock-in mice show an increased number of synaptic boutons/varicosities. In flies, hypomorphic and null mutations in Vap cause a severe decrease in numbers of varicosities and an increase in their size at the NMJs (25,43). Conversely, overexpression of drosophila Vap and human VAPB in *Drosophila* neurons induces a highly significant increase in the number of varicosities (43), similarity to what we observed in the ALS8 knock-in mice. The data suggests that ALS8 mutation might cause a gain of function in the NMJs, although there is a difference in neurotransmitter, receptors and molecular signals in *Drosophila* and mice NMJs (64). Notably, synaptic transmission is maintained in the *vap* null mutant flies and flies overexpressing human VAPB despite this structural alteration (43). Therefore, detailed studies are necessary to conclude how defects in morphology contribute to the pathology in ALS8.

A key observation in this study is that VAPB accumulates in the autophagosome in the motor neurons of the ALS8 knock-in mice, accompanying increased levels of P62/SQSTM1 and LC3 proteins. Significantly, other studies have implicated that defects in autophagic responses contribute to the pathology of ALS. Mutations in autophagy related genes including optineurin, P62/SQSTM1 and TBK1 are found in familial forms of ALS (5,65). P62/SQSTM1 accumulates in motor neurons in ALS patients (66,67), indicating that autophagic responses might be implicated in the common and core pathology of ALS. Neuronal autophagy has been shown to have a protective role under normal conditions. Its loss in mice deficient for the genes essential for autophagy, ATG5 and ATG7, causes neurodegeneration characterized by the widespread accumulation of cytoplasmic inclusions positive for ubiquitinated proteins (68,69). Hence, in ALS8, accumulation of P62/SQSTM1 and LC3 might function as a protective event (51). Alternatively, upregulation of autophagic responses might induce detrimental defects in ALS8 as observed in other neurodegenerative diseases (70). Autophagic responses might also be a result of ER stress (70,71), leading to the core pathology of ALS8.

This knock-in mouse replicates numerous aspects of the human disease, from progressive motor defects to selective motor neuron cellular pathology. Not only will this model allow us to study the mechanism of these varied deficits *in vivo*, but it provides a more authentic means of testing interventional therapies. These mice could be used, for example, to test the efficacy of compounds that have proven effective in other model organisms on facets of the phenotypes of motor neuron diseases or ALS.

Materials and Methods

Animals

Generation of P56S *Vapb* knock-in mice: we introduced P56S mutation into the *Vapb* locus using homologous recombination in ES cells and screened the targeted ES cells by Southern analysis (Supplementary Material, Fig. S1B) (72). We generated chimeric mice by microinjection of correctly targeted ES cells into 129 Sv/Ev blastocysts and mated the chimeric mice to 129 Sv/Ev females. We confirmed germ line transmission of the targeted allele carrying the P56S mutation by Southern analysis (Supplementary Material, Fig. S1B), PCR and direct sequencing of the mutation in the *Vapb* gene. The primers used for PCR are 5′-gtcccttcactgatgttgtcaccaccaac-3′ and 5′-aattctgcagcggctggctactaaggtac-3′. We removed neomycin resistance gene by breeding the P56S *Vapb* mutant mice with mice expressing Cre under the control of human cytomegalovirus (CMV) minimal promoter (73). Crosses between F1 mice carrying the P56S mutation in the *Vapb* allele produced wild-type ($Vapb^{WT}$), heterozygous ($Vapb^{WT/P56S}$) and homozygous ($Vapb^{P56S}$).

Generation of C57Bl6 mice with targeted disruption of *Vapb* gene: ES cells carrying gene trap cassette in the *Vapb* gene were created at the Texas A&M Institute for Genomic Medicine as previously described (46). The procedures for injecting, selecting and growing mouse ES cells have been described (74). We generated chimeric mice by microinjection of correctly targeted ES cells into C57BL/6 mice blastocysts and mated the chimeric mice to C57BL/6 females. The heterozygous mice were crossed to C57BL/6NCrl strain bred to each other and the litter genotyped by PCR. The following primers were used for genotyping. $Vapb^{GT}$ gene: 5′-cttgcaaaatggcgttaagc-3′ and 5′-cagatgcttagtgtgaacaagacccaagc-3′. $Vapb^{WT}$ gene: 5′-cttctgatatggaggcagtaagtacg-3′ and 5′-cagatgcttagtgtgaacaagacccaagc-3′. A 440 and 380 bp fragments were amplified separately in wild-type and $Vapb^{GT}$ genes. All mice were bred and maintained at the Canadian Council on Animal Care (CCAC)-accredited animal facilities of the Montreal Neurological Institute according to the CCAC guidelines. Mice were housed in an enriched environment with continuous access to food and water, under constant temperature and humidity, on a 12-h light/dark cycle. Approval for the animal experimentation was granted by the Animal Care and Use Committee of the McGill University.

RNA expression

Quantification of mouse *Vapb*, *Atf4*, *Atf6* and *CHOP* mRNA in mouse tissues was performed using The Viia7 qPCR instrument (Life Technologies). Total RNA was isolated from mouse tissues using RNeasy kit (#74104, Qiagen, CA, USA) according to the manufacturer's protocol and reverse-transcribed to cDNA using random primers and SuperScript® III reverse transcriptase (Invitrogen). Relative expression (RQ) was calculated using the SDS 2.2.2 software (Applied Biosystems). HPRT mRNA was used as a reference control. Primers used : gaaggtgatggaagagtgcag (*Vapb* Forward)—cccgaagtccgtcttcttc (*Vapb* Reverse)—cacgtcgattatat catgttgaaga (*CHOP* Forward)—gcacttccttctggaacactct (*CHOP*

Reverse)—tcagacaccggcaaggag (*Atf4* Forward)—tcatccaacgtggtcaagag (*Atf4* Reverse)—ccaccagaagtatgggttcg (*Atf6* Forward)—ggttctttatcatccgctgct (*Atf6* Reverse).

Protein expression and extraction analysis

Proteins were extracted from the spinal cord in RIPA buffer (50 mM Tris–HCl pH8, 150 mM NaCl, 1 mM EDTA, 1%NP40, 0.5% Sodium deoxycholate, 0.1% SDS) containing Complete (Roche) proteinase inhibitors and 1 mM PMSF. After homogenization, samples were spun at 20 000 g in a microcentrifuge, and supernatant was used for the soluble fraction. The insoluble pellet was dissolved in a buffer containing 8 M urea, 4% SDS, 0.125 M Tris–HCl (pH 6.8), 12 mM EDTA, 3% β-mercaptoethanol and 0.002% bromophenol blue; incubated at 65°C for 10 min; and subjected to SDS-PAGE. Western blot analysis was performed as previously described. Nitrocellulose blots were probed with rabbit polyclonal anti-Vap (1:5000) (33), guinea pig anti-p62/SQSTM (GP62-C, Progen, 1:2000), rabbit anti-phosphorylated eIF2α (SAB4504388, Sigma, 1/1000), mouse anti-eIF2α (L57A5, Cell Signaling Technology, 1/1000) and anti β-Actin (GT5412, Genetex, 1:20,000) antibodies.

Immunofluorescence

Immunofluorescence staining was performed as previously described (75). The following antisera were used for immunofluorescence of brain and spinal cord: rabbit anti-hVAPB(1:5000) (33); mouse anti-NeuN (MA377, Millipore, 1:300); rabbit anti-NeuN (ABN78, Millipore, 1:2000); rat anti-KDEL (ab50601, Abcam 1:50); rabbit anti-calreticulin (ADI-SPA-600, Enzo Life Science, 1:500); mouse anti-choline acetyltransferase (ChAT, ab35948, Abcam, 1/500); anti-Calbindin (C9848, Sigma, 1/1000); mouse anti-Ubiquitin (FK1, BML-PW8805-0500, Enzo Life Science, 1/100); rabbit anti-rat anti-CTIP2 (ab18465, Abcam, 1/500); mouse anti-BiP/GRP78 (sc-1050, Santa-Cruz, 1/50); mouse anti-LC3 (ab168803, Abcam, 1/10); mouse anti-PDI (1D3, Enzo Life Sciences, 1/100).

Behavioral analysis

Rotarod test: A cohort of 24 female mice was tested at 7, 11 and 15 months old. The locomotor activity was assessed in a bank of eight Versamax Animal Activity Monitor chambers (Accuscan Model RS2USB v4.00, Columbus, OH, USA). On the first day, mice were trained for three trials of 120 s. Testing was conducted on the next three consecutive days; each mouse was administered three trials each with a maximum duration of 300 s. The start speed was 4 RPM and was increased to a maximum speed of 25 RPM. The time mice spent on the rod without falling was recorded. Behavioral scores were subjected to statistical analysis using ANOVA with repeated measures.

Inverted grid test: for each trial, the mouse was put on the grid (bars spaced 1.5 cm apart) in a vertical position, the grid was then reversed upside down at a height of 25 cm above a padded cushion. The latency until the animal fell from the grid was recorded, the cut-off time was 5 min.

Open-field test: mice were individually placed into a chamber and locomotor activity was then recorded for a period of 90 consecutive minutes. All activities were recorded by a Versamax data analyzer (Accuscan Model VMX 1.4B, Columbus, OH, USA) and quantified using the Versamax Software System (Version 4.00, Accuscan, Columbus, OH, USA). The distance moved (in cm), time moving, number of discrete movement bouts (periods of movement separated by a minimum of 1 s of inactivity), stereotype time (time in which the animal repeatedly broke the same photocell beams) and stereotypy bouts (periods of stereotypy separated by a minimum of 1 s) were recorded in 10 min intervals.

NMJ analysis

Soleus muscles were dissected as previously described (42). Nerve terminals were labeled overnight at 4°C with mouse IgG anti-synaptic vesicular protein 2 (SV2, 1/500, Developmental Studies Hybridoma Bank). The muscles were then washed and incubated for 1 h at room temperature in anti-mouse Alexa 488 (1/1000, Cedarlane Laboratories Ltd). Post-synaptic nicotinic AChRs were then labeled with Alexa-594-conjugated-α-bungarotoxin (1/5000, 0.5 µg/ml, Invitrogen) for 30–45 min at room temperature. Antibodies were diluted in PBS containing 0.01% Triton X-100 and 2% normal donkey serum. Washing steps were done in PBS with 0.01% Triton X-100. Z-stacks were acquired with an LSM Zeiss 710 microscope. Morphological analysis was performed using ImageJ software. NMJ denervation was assessed by observing α-bungarotoxin/SV2 labeling coverage, incomplete coverage was noted as partial denervation. Faint clustered AChR corresponded to a faint α-bungarotoxin signal displaying a lack or organization. Ectopic AChR were two AChR groups present on the same muscle fiber and separated by more than 5 µm (42). NMJs presenting more than five post-synaptic fragments were considered fragmented. A continuous patch of α-bungarotoxin staining was considered as one fragment. The number of synaptic boutons was assessed by counting distinct pre-synaptic SV2 labeled zones. Size of boutons was assessed by measuring the total surface of SV2 labeling (Threshold and Measuring tool in ImageJ) and dividing it by the number of boutons. Total endplate area was calculated by tracing a perimeter encompassing all post-synaptic clusters (40). Statistical analyses were done on JMP 11 software. All analyses were done with one-way ANOVA followed by a post-hoc Multiple student *t*-test when necessary. Data in figures are presented as average ± SEM ($N = 3$ female animals per genotype, $n = 30$ NMJs for each genotype).

Histochemistry

Muscle histology—Gastrocnemius and soleus muscles were dissected and frozen in liquid nitrogen-cooled isopentane. 10 µm transverse cryostat sections were prepared on Snowcoat X-tra slides (Surgipath) and processed following standard Hematoxylin-Eosin or esterase staining protocols.

Spinal motor neurons quantification—30 µm transverse cryostat sections of L5 segments of mice spinal cords were mounted onto Snowcoat X-tra slides (Surgipath) and stained with Cresyl Violet for Nissl staining. Motor neurons from 10 sections/animal ($N = 3$ animals per genotype) were quantified.

Supplementary Material

Supplementary Material is available at *HMG* online.

Acknowledgements

We thank S. Lev and L. Dupuis for anti-VAPB antibodies. We also thank Éric Martineau for technical help in NMJs analysis.

Conflict of Interest statement. None declared.

Funding

H.T. was supported by grants from the Canadian Institutes of Health Research (MOP-115153).

References

1. Kiernan, M.C., Vucic, S., Cheah, B.C., Turner, M.R., Eisen, A., Hardiman, O., Burrell, J.R. and Zoing, M.C. (2011) Amyotrophic lateral sclerosis. *Lancet*, **377**, 942–955.
2. Rosen, D.R., Siddique, T., Patterson, D., Figlewicz, D.A., Sapp, P., Hentati, A., Donaldson, D., Goto, J., O'Regan, J.P., Deng, H. X. *et al.* (1993) Mutations in Cu/Zn superoxide dismutase gene are associated with familial amyotrophic lateral sclerosis. *Nature*, **362**, 59–62.
3. Sreedharan, J., Blair, I.P., Tripathi, V.B., Hu, X., Vance, C., Rogelj, B., Ackerley, S., Durnall, J.C., Williams, K.L., Buratti, E. *et al.* (2008) TDP-43 mutations in familial and sporadic amyotrophic lateral sclerosis. *Science*, **319**, 1668–1672.
4. Kwiatkowski, T.J. Jr., Bosco, D.A., Leclerc, A.L., Tamrazian, E., Vanderburg, C.R., Russ, C., Davis, A., Gilchrist, J., Kasarskis, E. J., Munsat, T. *et al.* (2009) Mutations in the FUS/TLS gene on chromosome 16 cause familial amyotrophic lateral sclerosis. *Science*, **323**, 1205–1208.
5. Fecto, F., Yan, J., Vemula, S.P., Liu, E., Yang, Y., Chen, W., Zheng, J.G., Shi, Y., Siddique, N., Arrat, H. *et al.* (2011) SQSTM1 mutations in familial and sporadic amyotrophic lateral sclerosis. *Arch. Neurol.*, **68**, 1440–1446.
6. Renton, A.E., Majounie, E., Waite, A., Simon-Sanchez, J., Rollinson, S., Gibbs, J.R., Schymick, J.C., Laaksovirta, H., van Swieten, J.C., Myllykangas, L. *et al.* (2011) A hexanucleotide repeat expansion in C9ORF72 is the cause of chromosome 9p21-linked ALS-FTD. *Neuron*, **72**, 257–268.
7. DeJesus-Hernandez, M., Mackenzie, I.R., Boeve, B.F., Boxer, A. L., Baker, M., Rutherford, N.J., Nicholson, A.M., Finch, N.A., Flynn, H., Adamson, J. *et al.* (2011) Expanded GGGGCC hexanucleotide repeat in noncoding region of C9ORF72 causes chromosome 9p-linked FTD and ALS. *Neuron*, **72**, 245–256.
8. DeJesus-Hernandez, M., Desaro, P., Johnston, A., Ross, O.A., Wszolek, Z.K., Ertekin-Taner, N., Graff-Radford, N.R., Rademakers, R. and Boylan, K. (2011) Novel p.Ile151Val mutation in VCP in a patient of African American descent with sporadic ALS. *Neurology*, **77**, 1102–1103.
9. Wong, P.C., Pardo, C.A., Borchelt, D.R., Lee, M.K., Copeland, N. G., Jenkins, N.A., Sisodia, S.S., Cleveland, D.W. and Price, D.L. (1995) An adverse property of a familial ALS-linked SOD1 mutation causes motor neuron disease characterized by vacuolar degeneration of mitochondria. *Neuron*, **14**, 1105–1116.
10. Joyce, P.I., Fratta, P., Fisher, E.M. and Acevedo-Arozena, A. (2011) SOD1 and TDP-43 animal models of amyotrophic lateral sclerosis: recent advances in understanding disease toward the development of clinical treatments. *Mamm. Genome*, **22**, 420–448.
11. Nishimura, A.L., Mitne-Neto, M., Silva, H.C., Oliveira, J.R., Vainzof, M. and Zatz, M. (2004) A novel locus for late onset amyotrophic lateral sclerosis/motor neurone disease variant at 20q13. *J. Med. Genet.*, **41**, 315–320.
12. Marques, V.D., Barreira, A.A., Davis, M.B., Abou-Sleiman, P.M., Silva, W.A. Jr., Zago, M.A., Sobreira, C., Fazan, V. and Marques, W. Jr. (2006) Expanding the phenotypes of the Pro56Ser VAPB mutation: proximal SMA with dysautonomia. *Muscle Nerve*, **34**, 731–739.
13. Kabashi, E., El Oussini, H., Bercier, V., Gros-Louis, F., Valdmanis, P.N., McDearmid, J., Mejier, I.A., Dion, P.A., Dupre, N., Hollinger, D. *et al.* (2013) Investigating the contribution of VAPB/ALS8 loss of function in amyotrophic lateral sclerosis. *Hum. Mol. Genet.*, **22**, 2350–2360.
14. Chattopadhyay, D. and Sengupta, S. (2014) First evidence of pathogenicity of V234I mutation of hVAPB found in Amyotrophic Lateral Sclerosis. *Biochem. Biophys. Res. Commun.*, **448**, 108–113.
15. Lev, S., Ben Halevy, D., Peretti, D. and Dahan, N. (2008) The VAP protein family: from cellular functions to motor neuron disease. *Trends Cell Biol.*, **18**, 282–290.
16. Nishimura, Y., Hayashi, M., Inada, H. and Tanaka, T. (1999) Molecular cloning and characterization of mammalian homologues of vesicle-associated membrane protein-associated (VAMP-associated) proteins. *Biochem. Biophys. Res. Commun.*, **254**, 21–26.
17. Weir, M.L., Klip, A. and Trimble, W.S. (1998) Identification of a human homologue of the vesicle-associated membrane protein (VAMP)-associated protein of 33kDa (VAP-33): a broadly expressed protein that binds to VAMP. *Biochem. J.*, **333** (Pt 2), 247–251.
18. Soussan, L., Burakov, D., Daniels, M.P., Toister-Achituv, M., Porat, A., Yarden, Y. and Elazar, Z. (1999) ERG30, a VAP-33-related protein, functions in protein transport mediated by COPI vesicles. *J. Cell. Biol.*, **146**, 301–311.
19. Kaiser, S.E., Brickner, J.H., Reilein, A.R., Fenn, T.D., Walter, P. and Brunger, A.T. (2005) Structural basis of FFAT motif-mediated ER targeting. *Structure*, **13**, 1035–1045.
20. Kosinski, M., McDonald, K., Schwartz, J., Yamamoto, I. and Greenstein, D. (2005) C. elegans sperm bud vesicles to deliver a meiotic maturation signal to distant oocytes. *Development*, **132**, 3357–3369.
21. Miller, M.A., Nguyen, V.Q., Lee, M.H., Kosinski, M., Schedl, T., Caprioli, R.M. and Greenstein, D. (2001) A sperm cytoskeletal protein that signals oocyte meiotic maturation and ovulation. *Science*, **291**, 2144–2147.
22. Tsuda, H., Han, S.M., Yang, Y., Tong, C., Lin, Y.Q., Mohan, K., Haueter, C., Zoghbi, A., Harati, Y., Kwan, J. *et al.* (2008) The amyotrophic lateral sclerosis 8 protein VAPB is cleaved, secreted, and acts as a ligand for Eph receptors. *Cell*, **133**, 963–977.
23. Han, S.M., Tsuda, H., Yang, Y., Vibbert, J., Cottee, P., Lee, S.J., Winek, J., Haueter, C., Bellen, H.J. and Miller, M.A. (2012) Secreted VAPB/ALS8 major sperm protein domains modulate mitochondrial localization and morphology via growth cone guidance receptors. *Dev. Cell*, **22**, 348–362.
24. Matsuzaki, F., Shirane, M., Matsumoto, M. and Nakayama, K.I. (2011) Protrudin serves as an adaptor molecule that connects KIF5 and its cargoes in vesicular transport during process formation. *Mol. Biol. Cell.*, **22**, 4602–4620.
25. Pennetta, G., Hiesinger, P.R., Fabian-Fine, R., Meinertzhagen, I.A. and Bellen, H.J. (2002) Drosophila VAP-33A directs bouton formation at neuromuscular junctions in a dosage-dependent manner. *Neuron*, **35**, 291–306.
26. Peretti, D., Dahan, N., Shimoni, E., Hirschberg, K. and Lev, S. (2008) Coordinated lipid transfer between the endoplasmic reticulum and the Golgi complex requires the VAP proteins and is essential for Golgi-mediated transport. *Mol. Biol. Cell.*, **19**, 3871–3884.
27. Kuijpers, M., Yu, K.L., Teuling, E., Akhmanova, A., Jaarsma, D. and Hoogenraad, C.C. (2013) The ALS8 protein VAPB interacts with the ER-Golgi recycling protein YIF1A and regulates membrane delivery into dendrites. *EMBO J.*, **32**, 2056–2072.
28. De Vos, K.J., Morotz, G.M., Stoica, R., Tudor, E.L., Lau, K.F., Ackerley, S., Warley, A., Shaw, C.E. and Miller, C.C. (2012) VAPB interacts with the mitochondrial protein PTPIP51 to regulate calcium homeostasis. *Hum. Mol. Genet.*, **21**, 1299–1311.
29. Kuijpers, M., van Dis, V., Haasdijk, E.D., Harterink, M., Vocking, K., Post, J.A., Scheper, W., Hoogenraad, C.C. and Jaarsma, D. (2013) Amyotrophic lateral sclerosis (ALS)-

associated VAPB-P56S inclusions represent an ER quality control compartment. *Acta Neuropathol. Commun.*, **1**, 24.
30. Aliaga, L., Lai, C., Yu, J., Chub, N., Shim, H., Sun, L., Xie, C., Yang, W.J., Lin, X., O'Donovan, M.J. *et al.* (2013) Amyotrophic lateral sclerosis-related VAPB P56S mutation differentially affects the function and survival of corticospinal and spinal motor neurons. *Hum. Mol. Genet.*, **22**, 4293–4305.
31. Tudor, E.L., Galtrey, C.M., Perkinton, M.S., Lau, K.F., De Vos, K. J., Mitchell, J.C., Ackerley, S., Hortobagyi, T., Vamos, E., Leigh, P.N. *et al.* (2010) Amyotrophic lateral sclerosis mutant vesicle-associated membrane protein-associated protein-B transgenic mice develop TAR-DNA-binding protein-43 pathology. *Neuroscience*, **167**, 774–785.
32. Qiu, L., Qiao, T., Beers, M., Tan, W., Wang, H., Yang, B. and Xu, Z. (2013) Widespread aggregation of mutant VAPB associated with ALS does not cause motor neuron degeneration or modulate mutant SOD1 aggregation and toxicity in mice. *Mol. Neurodegener.*, **8**, 1.
33. Amarilio, R., Ramachandran, S., Sabanay, H. and Lev, S. (2005) Differential regulation of endoplasmic reticulum structure through VAP-Nir protein interaction. *J. Biol. Chem.*, **280**, 5934–5944.
34. Smith, B. (1965) Changes in the enzyme histochemistry of skeletal muscle during experimental denervation and reinnervation. *J. Neurol. Neurosurg. Psychiatry*, **28**, 99–103.
35. Fischer, L.R., Culver, D.G., Tennant, P., Davis, A.A., Wang, M., Castellano-Sanchez, A., Khan, J., Polak, M.A. and Glass, J.D. (2004) Amyotrophic lateral sclerosis is a distal axonopathy: evidence in mice and man. *Exp. Neurol.*, **185**, 232–240.
36. Hegedus, J., Putman, C.T. and Gordon, T. (2007) Time course of preferential motor unit loss in the SOD1 G93A mouse model of amyotrophic lateral sclerosis. *Neurobiol. Dis.*, **28**, 154–164.
37. Dupuis, L. and Loeffler, J.P. (2009) Neuromuscular junction destruction during amyotrophic lateral sclerosis: insights from transgenic models. *Curr. Opin. Pharmacol.*, **9**, 341–346.
38. Cheng, A., Morsch, M., Murata, Y., Ghazanfari, N., Reddel, S.W. and Phillips, W.D. (2013) Sequence of age-associated changes to the mouse neuromuscular junction and the protective effects of voluntary exercise. *PloS One*, **8**, e67970.
39. Chipman, P.H., Franz, C.K., Nelson, A., Schachner, M. and Rafuse, V.F. (2010) Neural cell adhesion molecule is required for stability of reinnervated neuromuscular junctions. *Eur. J. Neurosci.*, **31**, 238–249.
40. Rudolf, R., Khan, M.M., Labeit, S. and Deschenes, M.R. (2014) Degeneration of neuromuscular junction in age and dystrophy. *Front. Aging Neurosci.*, **6**, 99.
41. Lichtman, J.W., Magrassi, L. and Purves, D. (1987) Visualization of neuromuscular junctions over periods of several months in living mice. *The J. Neurosci.*, **7**, 1215–1222.
42. Arbour, D., Tremblay, E., Martineau, E., Julien, J.P. and Robitaille, R. (2015) Early and persistent abnormal decoding by glial cells at the neuromuscular junction in an ALS model. *J. Neurosci.*, **35**, 688–706.
43. Chai, A., Withers, J., Koh, Y.H., Parry, K., Bao, H., Zhang, B., Budnik, V. and Pennetta, G. (2008) hVAPB, the causative gene of a heterogeneous group of motor neuron diseases in humans, is functionally interchangeable with its Drosophila homologue DVAP-33A at the neuromuscular junction. *Hum. Mol. Genet.*, **17**, 266–280.
44. Ratnaparkhi, A., Lawless, G.M., Schweizer, F.E., Golshani, P. and Jackson, G.R. (2008) A Drosophila model of ALS: human ALS-associated mutation in VAP33A suggests a dominant negative mechanism. *PLoS One*, **3**, e2334.
45. Hansen, G.M., Markesich, D.C., Burnett, M.B., Zhu, Q., Dionne, K.M., Richter, L.J., Finnell, R.H., Sands, A.T., Zambrowicz, B.P. and Abuin, A. (2008) Large-scale gene trapping in C57BL/6N mouse embryonic stem cells. *Genome Res.*, **18**, 1670–1679.
46. Zambrowicz, B.P., Abuin, A., Ramirez-Solis, R., Richter, L.J., Piggott, J., BeltrandelRio, H., Buxton, E.C., Edwards, J., Finch, R.A., Friddle, C.J. *et al.* (2003) Wnk1 kinase deficiency lowers blood pressure in mice: a gene-trap screen to identify potential targets for therapeutic intervention. *Proc. Natl. Acad. Sci. USA*, **100**, 14109–14114.
47. Teuling, E., Ahmed, S., Haasdijk, E., Demmers, J., Steinmetz, M.O., Akhmanova, A., Jaarsma, D. and Hoogenraad, C.C. (2007) Motor neuron disease-associated mutant vesicle-associated membrane protein-associated protein (VAP) B recruits wild-type VAPs into endoplasmic reticulum-derived tubular aggregates. *J. Neurosci.*, **27**, 9801–9815.
48. Tjoelker, L.W., Seyfried, C.E., Eddy, R.L. Jr., Byers, M.G., Shows, T.B., Calderon, J., Schreiber, R.B. and Gray, P.W. (1994) Human, mouse, and rat calnexin cDNA cloning: identification of potential calcium binding motifs and gene localization to human chromosome 5. *Biochemistry*, **33**, 3229–3236.
49. Vaux, D., Tooze, J. and Fuller, S. (1990) Identification by anti-idiotype antibodies of an intracellular membrane protein that recognizes a mammalian endoplasmic reticulum retention signal. *Nature*, **345**, 495–502.
50. Matsumoto, S., Hirano, A. and Goto, S. (1990) Ubiquitin-immunoreactive filamentous inclusions in anterior horn cells of Guamanian and non-Guamanian amyotrophic lateral sclerosis. *Acta Neuropathol.*, **80**, 233–238.
51. Bjorkoy, G., Lamark, T., Brech, A., Outzen, H., Perander, M., Overvatn, A., Stenmark, H. and Johansen, T. (2005) p62/SQSTM1 forms protein aggregates degraded by autophagy and has a protective effect on huntingtin-induced cell death. *J. Cell. Biol.*, **171**, 603–614.
52. Bjorkoy, G., Lamark, T., Pankiv, S., Overvatn, A., Brech, A. and Johansen, T. (2009) Monitoring autophagic degradation of p62/SQSTM1. *Methods Enzymol.*, **452**, 181–197.
53. Kabeya, Y., Mizushima, N., Yamamoto, A., Oshitani-Okamoto, S., Ohsumi, Y. and Yoshimori, T. (2004) LC3, GABARAP and GATE16 localize to autophagosomal membrane depending on form-II formation. *J. Cell Sci.*, **117**, 2805–2812.
54. Manford, A.G., Stefan, C.J., Yuan, H.L., Macgurn, J.A. and Emr, S.D. (2012) ER-to-plasma membrane tethering proteins regulate cell signaling and ER morphology. *Dev. Cell*, **23**, 1129–1140.
55. Moustaqim-Barrette, A., Lin, Y.Q., Pradhan, S., Neely, G.G., Bellen, H.J. and Tsuda, H. (2014) The amyotrophic lateral sclerosis 8 protein, VAP, is required for ER protein quality control. *Hum. Mol. Genet.*, **23**, 1975–1989.
56. Lee, A.H., Iwakoshi, N.N. and Glimcher, L.H. (2003) XBP-1 regulates a subset of endoplasmic reticulum resident chaperone genes in the unfolded protein response. *Mol. Cell. Biol.*, **23**, 7448–7459.
57. Morris, J.A., Dorner, A.J., Edwards, C.A., Hendershot, L.M. and Kaufman, R.J. (1997) Immunoglobulin binding protein (BiP) function is required to protect cells from endoplasmic reticulum stress but is not required for the secretion of selective proteins. *J. Biol. Chem.*, **272**, 4327–4334.
58. Prostko, C.R., Brostrom, M.A. and Brostrom, C.O. (1993) Reversible phosphorylation of eukaryotic initiation factor 2 alpha in response to endoplasmic reticular signaling. *Mol. Cell. Biochem.*, **127–128**, 255–265.
59. Harding, H.P., Novoa, I., Zhang, Y., Zeng, H., Wek, R., Schapira, M. and Ron, D. (2000) Regulated translation initiation controls

stress-induced gene expression in mammalian cells. *Mol. Cell*, **6**, 1099–1108.
60. Anagnostou, G., Akbar, M.T., Paul, P., Angelinetta, C., Steiner, T.J. and de Belleroche, J. (2008) Vesicle associated membrane protein B (VAPB) is decreased in ALS spinal cord. *Neurobiol. Aging*, **31**, 969–985.
61. Atkin, J.D., Farg, M.A., Turner, B.J., Tomas, D., Lysaght, J.A., Nunan, J., Rembach, A., Nagley, P., Beart, P.M., Cheema, S.S. *et al.* (2006) Induction of the unfolded protein response in familial amyotrophic lateral sclerosis and association of protein-disulfide isomerase with superoxide dismutase 1. *J. Biol. Chem.*, **281**, 30152–30165.
62. Atkin, J.D., Farg, M.A., Walker, A.K., McLean, C., Tomas, D. and Horne, M.K. (2008) Endoplasmic reticulum stress and induction of the unfolded protein response in human sporadic amyotrophic lateral sclerosis. *Neurobiol. Dis.*, **30**, 400–407.
63. Sasaki, S. (2010) Endoplasmic reticulum stress in motor neurons of the spinal cord in sporadic amyotrophic lateral sclerosis. *J. Neuropathol. Exp. Neurol.*, **69**, 346–355.
64. Wu, H., Xiong, W.C. and Mei, L. (2010) To build a synapse: signaling pathways in neuromuscular junction assembly. *Development*, **137**, 1017–1033.
65. Cirulli, E.T., Lasseigne, B.N., Petrovski, S., Sapp, P.C., Dion, P. A., Leblond, C.S., Couthouis, J., Lu, Y.F., Wang, Q., Krueger, B. J. *et al.* (2015) Exome sequencing in amyotrophic lateral sclerosis identifies risk genes and pathways. *Science*, **347**, 1436–1441.
66. Hiji, M., Takahashi, T., Fukuba, H., Yamashita, H., Kohriyama, T. and Matsumoto, M. (2008) White matter lesions in the brain with frontotemporal lobar degeneration with motor neuron disease: TDP-43-immunopositive inclusions co-localize with p62, but not ubiquitin. *Acta Neuropathol.*, **116**, 183–191.
67. Mizuno, Y., Amari, M., Takatama, M., Aizawa, H., Mihara, B. and Okamoto, K. (2006) Immunoreactivities of p62, an ubiqutin-binding protein, in the spinal anterior horn cells of patients with amyotrophic lateral sclerosis. *J. Neurol. Sci.*, **249**, 13–18.
68. Hara, T., Nakamura, K., Matsui, M., Yamamoto, A., Nakahara, Y., Suzuki-Migishima, R., Yokoyama, M., Mishima, K., Saito, I., Okano, H. *et al.* (2006) Suppression of basal autophagy in neural cells causes neurodegenerative disease in mice. *Nature*, **441**, 885–889.
69. Komatsu, M., Waguri, S., Chiba, T., Murata, S., Iwata, J.I., Tanida, I., Ueno, T., Koike, M., Uchiyama, Y., Kominami, E. *et al.* (2006) Loss of autophagy in the central nervous system causes neurodegeneration in mice. *Nature*, **441**, 880–884.
70. Jaeger, P.A. and Wyss-Coray, T. (2009) All-you-can-eat: autophagy in neurodegeneration and neuroprotection. *Mol. Neurodegener.*, **4**, 16.
71. Kapuy, O., Vinod, P.K. and Banhegyi, G. (2014) mTOR inhibition increases cell viability via autophagy induction during endoplasmic reticulum stress—an experimental and modeling study. *FEBS Open Bio.*, **4**, 704–713.
72. Abuin, A. and Bradley, A. (1996) Recycling selectable markers in mouse embryonic stem cells. *Mol. Cell. Biol.*, **16**, 1851–1856.
73. Su, H., Mills, A.A., Wang, X. and Bradley, A. (2002) A targeted X-linked CMV-Cre line. *Genesis*, **32**, 187–188.
74. Zambrowicz, B.P., Friedrich, G.A., Buxton, E.C., Lilleberg, S.L., Person, C. and Sands, A.T. (1998) Disruption and sequence identification of 2,000 genes in mouse embryonic stem cells. *Nature*, **392**, 608–611.
75. Tsuda, H., Jafar-Nejad, H., Patel, A.J., Sun, Y., Chen, H.K., Rose, M.F., Venken, K.J., Botas, J., Orr, H.T., Bellen, H.J. *et al.* (2005) The AXH domain of Ataxin-1 mediates neurodegeneration through its interaction with Gfi-1/Senseless proteins. *Cell*, **122**, 633–644.